Zhao, S. *et al*. (2018). *Géotechnique* **68**, No. 12, 1085–1098 [https://doi.org/10.1680/jgeot.17.P.158]

Effects of curvature-related DEM contact model on the macro- and micro-mechanical behaviours of granular soils

S. ZHAO*†, T. M. EVANS† and X. ZHOU*‡

A comprehensive comparison between the Hertz–Mindlin model and the linear spring model in true triaxial shear simulations of granular soils was conducted using the discrete-element method (DEM). The no-slip Hertz–Mindlin model for general elastic non-spherical particles with smooth surfaces was revisited and implemented for superellipsoidal particles in an in-house DEM code. Three groups of specimens with a grain size distribution of Ottawa 20–30 sands, consisting of spheres, ellipsoids and superellipsoids, respectively, were subjected to triaxial shear DEM simulations with the Hertz–Mindlin model and the linear spring model. The corresponding mechanical behaviours were examined in terms of a series of macro- and micro-parameters. It was found that the linear spring model was able to resemble the Hertz–Mindlin model in aspects of both microscopic and macroscopic mechanical behaviours of granular media with spherical and/or non-spherical particles. This finding suggests that the linear spring model can be used to investigate micro-mechanical behaviours of granular soils, even with complex particle shapes.

KEYWORDS: discrete-element modelling; fabric/structure of soils; particle-scale behaviour; statistical analysis

INTRODUCTION

Granular soils, composed of discrete solid particles interacting with one another, have complex physical and mechanical behaviours (Herrmann *et al*., 2013). It is well known that continuum constitutive models of macroscopic behaviour cannot fully describe the mechanical behaviours of granular soils owing to their internally discontinuous nature. Therefore, it is meaningful to develop an understanding of the strength and deformation mechanisms of granular soils from a particle-scale (often referred to as microscopic) point of view. Accordingly, there has been a growing interest in numerical investigations in geomechanics using the discrete-element method (DEM, Cundall & Strack (1979)) to simulate, for example, conventional direct shear tests and triaxial compression tests (Cui & O'Sullivan, 2006; Cui *et al*., 2007). The interested reader is referred to O'Sullivan (2011) for a good review of the application of the DEM in geomechanics.

Although the DEM is a powerful numerical tool for particulate investigations in geomechanics, DEM models in practice are usually considerably simplified in aspects of particle shape and the inter-particle contact model. Specifically, soil particles are modelled using idealised spheres instead of complex shapes, and a simple linear spring (LS) model is adopted instead of a more complicated non-linear model (typically the Hertz–Mindlin (HM) model (Johnson, 1985)) – for example, Zhao & Evans (2011), Zhao & Guo (2013), Zhao *et al*. (2017a). Both simplifications contribute to speeding up simulations (O'Sullivan, 2011), but inevitably there is some loss in modelling accuracy. In particular, the significance of particle shape on the mechanical behaviours of granular soils has been reported in many experimental investigations – for example, by Cho *et al*. (2006) and Shin & Santamarina (2012). To indirectly consider the effect of particle shape in simulations of spheres, rolling resistance (Iwashita & Oda, 1998; Jiang *et al*., 2015) is sometimes artificially introduced in the contact model to obtain comparable macroscopic behaviours of granular soils. Such a workaround can definitely reduce computational cost; however, the internal fabric of granular soils is less realistic (Zhou *et al*., 2013). Indeed, the effect of particle shape on the granular fabric is significant (Zhao *et al*., 2017b).

In the DEM, particles are assumed to be perfectly rigid without deformation, but allowed to overlap (i.e. the so-called 'soft-contact' approach). As a consequence, contact force can be calculated from the overlap in terms of a given contact model. Generally, the normal and shear contact forces F_n and F_s are calculated using a force–displacement law (Cundall & Strack, 1979; Potyondy & Cundall, 2004) given as

$$F_n = K_n \delta \tag{1a}$$

$$F_s = F_s' - k_s \Delta u \tag{1b}$$

where K_n is the contact normal-secant stiffness; k_s is the contact shear-tangent stiffness; δ is the contact penetration depth; Δu is the incremental shear displacement during the current time step; and F_s' is the shear contact force at the previous time step. Note here that $K_n = 2k_n/3$ for the HM model, whereas $K_n = k_n$ for the LS model, where k_n is the contact normal-tangent stiffness. Theoretically, the contact stiffnesses k_n and k_s are related to the material properties, contact geometric deformation and loading history. The HM model describes a more realistic contact behaviour than the LS model (Johnson, 1985).

With respect to the LS model, particle contact stiffnesses k_n and k_s are arbitrarily specified without a universal criterion, even for spherical particles. For example,

Manuscript received 16 June 2017; revised manuscript accepted 23 January 2018. Published online ahead of print 7 March 2018. Discussion on this paper closes on 1 May 2019, for further details see p. ii.

* State Key Laboratory of Subtropical Building Science, South China University of Technology, Guangzhou, P. R. China.
† School of Civil and Construction Engineering, Oregon State University, Corvallis, OR, USA.
‡ Powerchina Huadong Engineering Corporation Limited, Hangzhou, P. R. China.

Potyondy & Cundall (2004) established a bonded-particle model in which the particle normal stiffness k_n correlates with the particle radius R and the Young's modulus E_c of the particle as $k_n = 4RE_c$. For simplicity, the normal and tangential contact stiffnesses are set directly – for example, $k_n/r = k_s/r = 100$ MPa (where r is the equivalent radius of two contacting particles) (Zhao & Guo, 2013). At other times, researchers have assigned the values of normal and tangential stiffness without a detailed explanation. With respect to the HM contact model, the ratio of tangential to normal stiffness k_s/k_n lies in [2/3, 1] (Goldenberg & Goldhirsch, 2005).

Researchers have proposed a variety of particle shapes for DEM simulations – for example, Lin & Ng (1997), Cleary (2008) and Eliáš (2014). A simple and direct solution is the so-called clump technique by which a complex particle shape is approximately constructed using spheres – for example, Garcia *et al.* (2009). However, this technique might produce some unrealistic multi-contacts in some cases (Höhner *et al.*, 2012). Moreover, the contact profile is always circular, independent of particle shape. In contrast, analytical geometric shapes are preferable to implement the HM model. However, the HM model is not applicable for some special cases – for example, polyhedral particles (Eliáš, 2014). The HM model involves computation of the principal curvatures, referred to as the curvature-related DEM contact model, which makes the computation more intensive. Thus, many researchers are likely to use the LS model – for example, Cleary (2008), Delaney & Cleary (2010), Langston *et al.* (2015) and Majidi *et al.* (2015).

A few studies on the comparison of the LS and HM models have been reported so far. For example, Di Renzo & Di Maio (2004) compared the LS and HM models for the simulation of particle collisions. Thornton *et al.* (2013) analysed the effect of the LS and HM models on the rebound characteristics in simulating the inelastic oblique impact of a sphere against a wall. Non-spherical particles have been investigated even less. A preliminary investigation shows that specimens using the LS model and the HM model share qualitatively similar macro-mechanical behaviours (Wellmann *et al.*, 2008). However, it is still an open issue to answer whether using the LS model is capable of yielding similar results as using the HM model when investigating macro- and micro-mechanical behaviours of granular soils considering the particle shape effect. This idea is explored further herein.

SIMULATION SET-UP

DEM contact models

Hertz–Mindlin is a well-known model in contact mechanics. An overview may be found in many textbooks – for example, Johnson (1985) and Santamarina *et al.* (2001). Referring to the derivation in Appendix 1, the contact normal-tangent stiffness k_n is given as

$$k_n = \frac{2\pi}{\alpha}\sqrt{\frac{E'}{K'^3(A+B)}}G^*\delta^{1/2} \tag{2}$$

where the symbols are introduced in Appendix 1, and the contact normal-secant stiffness, $K_n = 2k_n/3$.

With Mindlin's no-slip solutions, for simplicity, it is assumed that the tangential force is parallel to the tangential displacement, and $k_s = (k_x + k_y)/2$ where k_x and k_y are principal shear tangent stiffnesses given later by equations (23) and (24). A similar simplification has been employed by other researchers – for example, Lin & Ng (1997) and Wellmann *et al.* (2008). It can be verified that k_x/k_y ($k_x \geq k_y$) lies in [1, 2] for practical Poisson ratios $\nu \leq 0{\cdot}5$.

For two spheres in contact, with radii of R_1 and R_2, the contact profile degenerates to a circle. Therefore, k_n and k_s are simplified as

$$k_n = \frac{4}{\mu_1 - \mu_2}\sqrt{\frac{R_1R_2\delta}{R_1+R_2}} \tag{3}$$

$$k_s = \frac{8}{2\mu_1 - \mu_2}\sqrt{\frac{R_1R_2\delta}{R_1+R_2}} \tag{4}$$

Equations (3) and (4) after substituting μ_1 and μ_2 are in agreement with those of Cundall's derivation (Cundall, 1988) applied in the commercial software, *PFC*^{3D}. Considering two contacting bodies of the same material properties, the ratio of k_s to k_n is equal to $2(1-\nu)/(2-\nu)$, which lies in [2/3, 1] for practical Poisson ratios, $\nu \leq 0{\cdot}5$.

For the LS model, both normal and tangential contact stiffnesses are constant and set directly in simulations.

Superellipsoid-based DEM

Superellipsoids are able to capture the main geometric features of particles in nature (Williams & Pentland, 1992), and are employed to consider the effect of particle shape. A typical five-parameter surface function of a superellipsoid in the local Cartesian coordinates is given as (Barr, 1981)

$$\left(\left|\frac{x}{r_x}\right|^{2/\varepsilon_1} + \left|\frac{y}{r_y}\right|^{2/\varepsilon_2}\right)^{\varepsilon_1/\varepsilon_2} + \left|\frac{z}{r_z}\right|^{2/\varepsilon_2} = 1 \tag{5}$$

where r_x, r_y and r_z are referred to as the semi-major axis lengths in the directions of the x, y and z axes, respectively, and ε_i ($i = 1, 2$) are the shape parameters determining the sharpness of the particle edges. In this work, a special case is taken where $r_z = \eta r_x = \eta r_y$ and $\varepsilon = \varepsilon_1 = \varepsilon_2$ for simplicity, but it is noted that there is still a broad range of particle shapes available. Fig. 1 shows variation of particle shape with η and ε.

Given that the principal curvatures of a superellipsoid can be readily obtained (see Appendix 4), it is possible to install the HM model at the contact of two contacting superellipsoids. An in-house superellipsoid-based DEM code, *SudoDEM* (Zhao & Zhou, 2017; Zhao *et al.*, 2017b) is applied in this work, where the HM and LS models are implemented. Moreover, inter-particle sliding is modelled with a slip model where the tangential contact force complies with Coulomb's friction law.

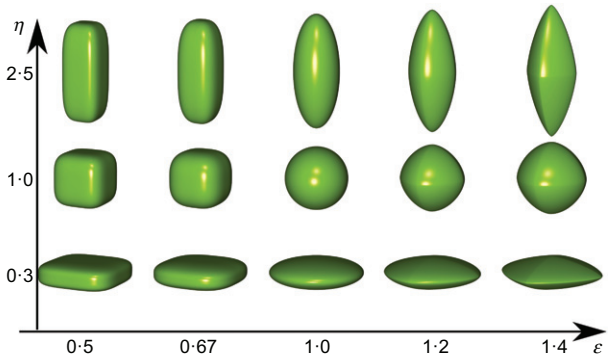

Fig. 1. Particle shapes varying with η and ε

Specimen preparation

Three groups of cubical specimens, denoted as G*i* ($i = 1, 2, 3$), are considered with different particle shapes, which share the same grain size distribution (GSD) similar to Ottawa 20–30 sands (see Fig. 2). The diameter of the sphere with the same volume of a non-spherical particle is taken as the particle's equivalent diameter. The geometric properties of particles within the three groups are summarised in Table 1. Each group consists of three specimens prepared using the HM and LS models, denoted as G*i*-HM, G*i*-LS1 and G*i*-LS2, respectively.

Specimens of each group are prepared with the following protocol. (*a*) Approximately 5000 particles with random positions and orientations are generated with an initial void ratio of 0·6 in a cubical container with six frictionless rigid walls, where the induced particle overlap is not considered; the system is allowed to cycle to equilibrium as excess kinetic energy is dissipated. Energy is dissipated by periodically setting the velocities of all particles to zero while the container walls remain fixed. (*b*) The assembly is subjected to isotropic compression with a stress of 100 kPa using the LS model. (*c*) The LS model in (*b*) is replaced by the HM model, yielding specimen G*i*-HM after consolidation. (*d*) With the configuration data from specimen G*i*-HM, specimens G*i*-LS1 and G*i*-LS2 are prepared using the LS model after consolidation. In this manner, the initial fabric of all assemblies is as consistent as possible. The consolidation procedure is implemented by way of a numerical stress-controlled servo algorithm (Zhao *et al*., 2015) to maintain a constant stress, σ_0, of 100 kPa on each specimen.

The material properties of particles in the DEM simulations are listed in Table 2. The local damping coefficient is set to 0·3. Density scaling is employed to reduce the computational cost associated with DEM simulations for quasi-static analyses, where the velocities and accelerations will be affected while contact forces and displacements are not sensitive to the density value used – for example, Thornton (2000) and Cui & O'Sullivan (2006). For the HM model in specimens G*i*-HM, the elastic properties are from quartz particles (Santamarina *et al*., 2001). For the LS model in specimens G*i*-LS1 and G*i*-LS2, it is assumed that the tangential contact stiffness is equal to the normal contact stiffness. In detail, in specimens G*i*-LS1 $k_n/r_0 = k_s/r_0 = 1$ GPa (r_0 is the average radius of particles), where k_n is equal to about the average of normal-secant stiffness within the consolidated specimens G*i*-HM, whereas for comparison $k_n/r_0 = k_s/r_0 = 100$ MPa is used in specimens G*i*-LS2, as assumed in the literature (Zhao & Guo, 2013). The inter-particle coefficient of friction μ_p is significantly dependent on the surface roughness. For example, Senetakis *et al*. (2013) reported μ_p varying between 0·093 and 0·231 for quartz particles, whereas Nardelli *et al*. (2017) reported μ_p ranging between 0·249 and 0·372. Here the μ_p of 0·3 is applied in the simulations. Moreover, the LS model with $K_n = 10^6$ N/m is installed at wall–particle contacts for all simulations to obtain comparable results. Nine specimens are prepared using the above procedure. Their basic characteristics are listed in Table 3.

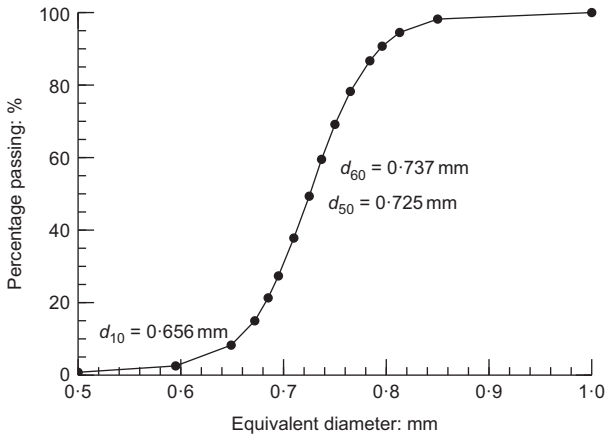

Fig. 2. Grain size distribution similar to Ottawa 20–30 sands

Table 1. Geometric properties of particles in the DEM specimens

Group	Particle shape	η	ε
G1	Sphere	1·0	1·0
G2	Ellipsoid	1·0∼1·5	1·0
G3	Superellipsoid	1·0∼1·5	0·5∼1·4

Table 2. Material properties of particles in the DEM simulations

Properties	G*i*-HM	G*i*-LS1	G*i*-LS2
Density: 10^6 kg/m^3	2650	2650	2650
Shear modulus, G: GPa	29	—	—
Poisson ratio, v	0·31	—	—
Normal stiffness, K_n: N/m	—	3×10^5	3×10^4
Tangential stiffness, k_s: N/m	—	3×10^5	3×10^4
Particle coefficient of friction	0·3	0·3	0·3

Triaxial compression tests

All prepared specimens are subjected to triaxial compression tests after consolidation. During triaxial compression, the top and bottom walls move towards each other at a constant loading strain rate of 0·01/s, which is sufficiently small to maintain quasistatic conditions with an inertial number of $6 \times 10^{-4} < 10^{-3}$ (Zhao & Zhou, 2017), whereas the other four side walls move individually to maintain a constant confining stress σ_0 of 100 kPa with the stress-control servo, as mentioned above. Compression stops at an axial strain of 40%. In the authors' experience, such an axial strain is sufficiently large to reach a critical state. More details about the triaxial compression procedure are presented in Zhao & Zhou (2017). Figs 3(a) and 3(b) show snapshots of specimens G*i*-HM before and after shearing, respectively; the other specimens are not shown because of the similar configurations of specimens G*i*-HM.

RESULTS AND DISCUSSION

Macroscopic strength and deformation

The macroscopic mechanical response of a granular material during shearing can be quantified by the stress

Table 3. Characteristics of specimens after consolidation

Specimen	Void ratio	Coordination number
G1-HM	0·644	5·186
G1-LS1	0·643	5·573
G1-LS2	0·633	5·867
G2-HM	0·597	5·322
G2-LS1	0·596	5·476
G2-LS2	0·583	6·163
G3-HM	0·488	5·858
G3-LS1	0·488	6·192
G3-LS2	0·481	6·931

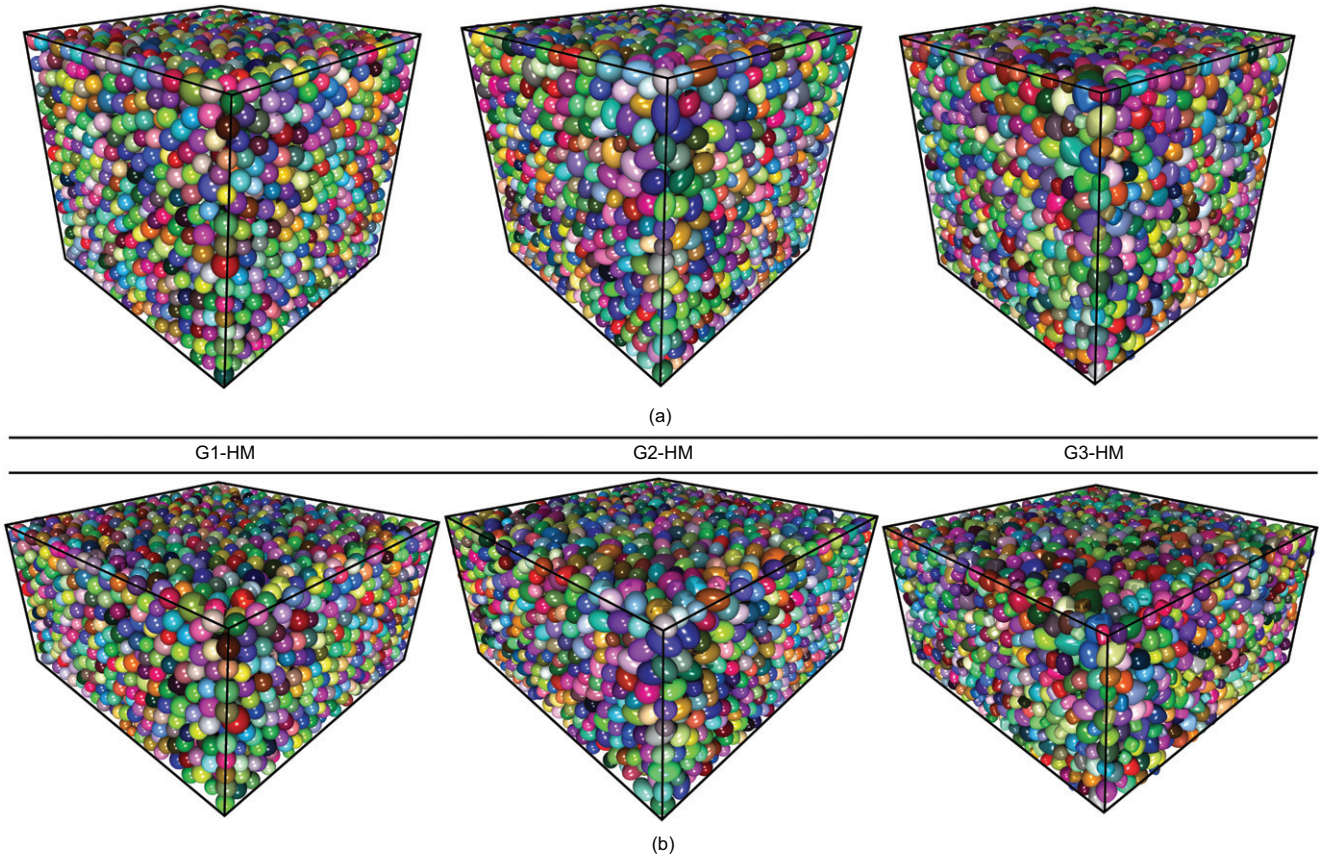

Fig. 3. Configurations of specimens G*i*-HM at (a) the initial and (b) the final states

tensor that is calculated from discrete measurements with the following definition proposed by (Christoffersen *et al.*, 1981)

$$\boldsymbol{\sigma}_{ij} = \frac{1}{V}\sum_{c\in V} f_i^{\mathrm{c}} \boldsymbol{l}_j^{\mathrm{c}} \tag{6}$$

where V is the total volume of the assembly; f^{c} is the contact force at the contact c; and $\boldsymbol{l}^{\mathrm{c}}$ is the branch vector joining the centres of the two contacting particles at contact c. The mean stress p and the deviatoric stress q are defined as

$$p = \frac{1}{3}\boldsymbol{\sigma}_{ii} \tag{7a}$$

$$q = \sqrt{\frac{3}{2}\sigma'_{ij}\sigma'_{ij}} \tag{7b}$$

where σ'_{ij} is the deviatoric part of stress tensor $\boldsymbol{\sigma}_{ij}$.

Given that the cubical specimens are confined by rigid walls, the axial strain ε_z and the volumetric strain ε_{v} can be approximately calculated from the positions of the boundary walls, that is

$$\boldsymbol{\epsilon}_z = \int_{H_0}^{H} \frac{\mathrm{d}h}{h} = -\ln\frac{H_0}{H} \tag{8a}$$

$$\boldsymbol{\epsilon}_v = \boldsymbol{\epsilon}_x + \boldsymbol{\epsilon}_y + \boldsymbol{\epsilon}_z = \int_{V_0}^{V} \frac{\mathrm{d}v}{v} = -\ln\frac{V_0}{V} \tag{8b}$$

where H and V are the height and volume of the specimen during shearing, respectively, and H_0 and V_0 are their initial values before shear. Positive values of volumetric strain represent dilatancy.

Figures 4(a)–4(c) show evolution of the deviatoric stress ratio q/p and volumetric strain ε_{v} for all three groups of specimens during shearing. It is evident that each specimen exhibits a peak stress followed by softening with a corresponding volumetric dilatation, which is similar to observed behaviours of dense sands in the laboratory. Moreover, both the deviatoric stress ratio and the volumetric strain approach steady values when reaching an axial strain of 30%. It is reasonable to say that all specimens reach critical states at an axial strain of 40%.

With respect to the effects of contact models, it can be seen that the responses of specimens G*i*-LS1 are consistent with those of specimens G*i*-HM, regardless of particle shape. In other words, using the LS model is able to yield similar macroscopic responses of granular soils as using the HM model. Moreover, specimens G*i*-LS2 show a similar stress–strain curve as specimens G*i*-HM and G*i*-LS1, even though the contact stiffness in specimens G*i*-LS2 is one order of magnitude less than that in specimens G*i*-LS1 and specimens G*i*-LS2 are slightly denser than the other counterpart specimens. This indicates that contact stiffness has a negligibly small effect on the shear strength of a granular material, as reported in the literature (Ng, 2006), where this feature is attributed to similar initial fabric. However, as shown in Fig. 5, contact stiffness has a considerable effect on the small-strain behaviours of a granular material, which has also been reported in the literature – for example, Yimsiri & Soga (2000). Note that the contact stiffness of interest varies within the range of one order of magnitude less than the benchmark. In contrast, a significant discrepancy in volumetric strains between specimens G*i*-LS2 and G*i*-LS1 is observed, implying that contact stiffness has a considerable effect on deformation of granular materials. Interestingly, it appears that particle shape has a

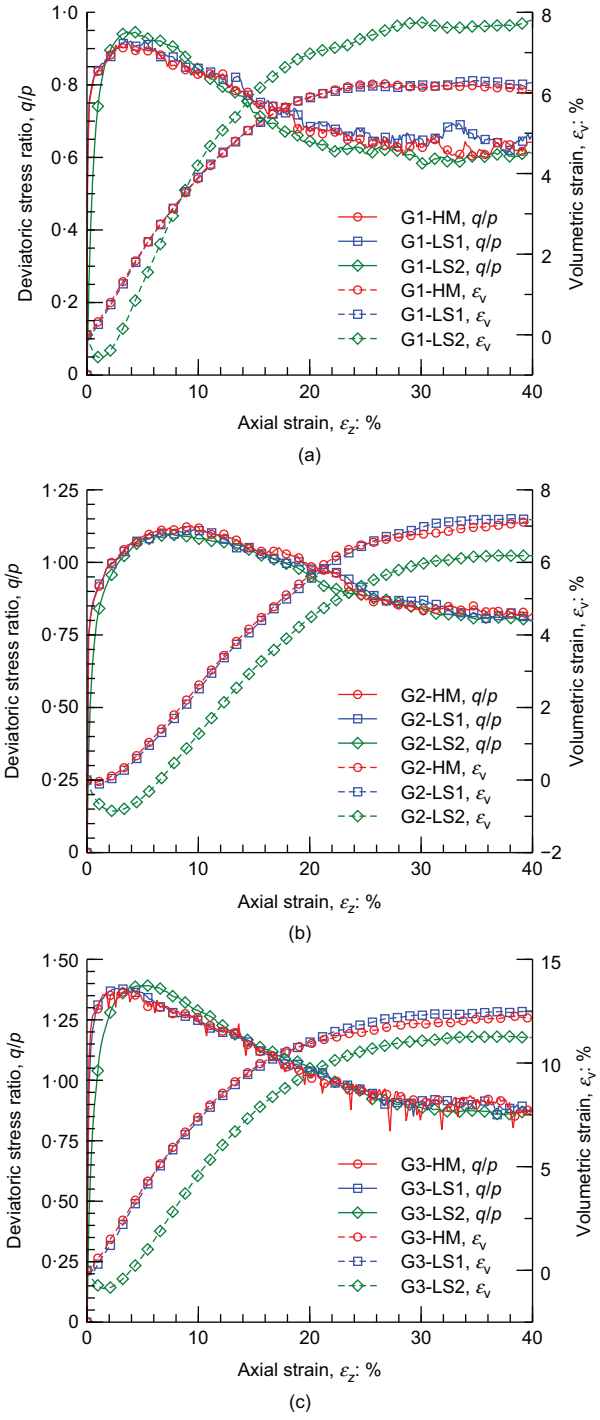

Fig. 4. Variation of deviatoric stress ratio *q/p* and volumetric strain ε_v with axial strain for all specimens during shearing: (a) G1; (b) G2; (c) G3

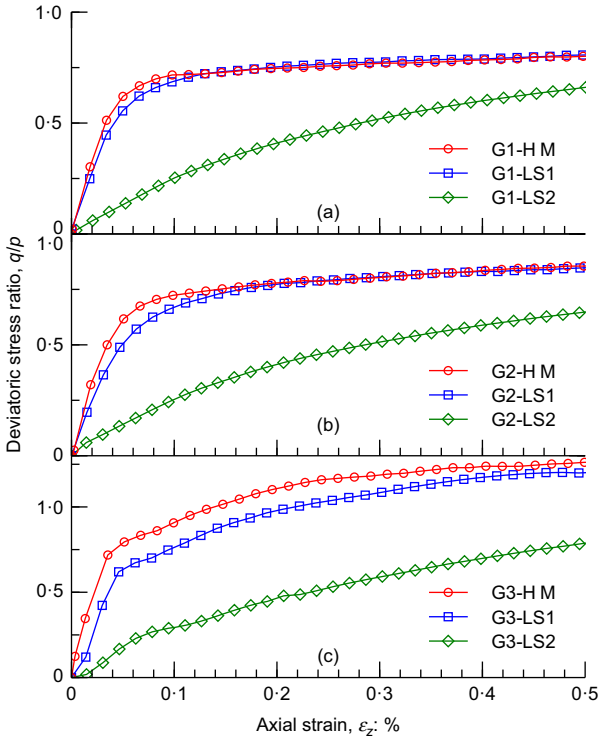

Fig. 5. Variation of deviatoric stress ratio *q/p* at small strains during shearing: (a) G1; (b) G2; (c) G3

considerably different effect on the deformation mechanism of specimens with softer contacts, where specimens G*i*-LS2 are less dilative than specimens G*i*-LS1 for non-spherical particles, whereas the contrary case is found for spherical particles.

With the procedure for specimen preparation discussed previously, the initial fabric of specimens in each group is controlled about the same, which is verified by similar void ratios and local void ratio distributions, as shown in the subsequent analysis. The following sections provide a comprehensive analysis of the initial fabric of each group of specimens. A series of microscopic parameters is employed to compare the effect of the HM and LS models.

Unsheared and sheared states

Contact stiffness distributions. Understanding the contact stiffness distributions within specimens G*i*-HM can provide a guide for selecting reasonable values of contact stiffness in the LS model. Here the focus is placed on the normal-secant stiffness K_n and shear-tangential stiffness k_s. The probability distributions of K_n and k_s are shown in Figs 6(a)–6(c) and 6(d)–6(f), respectively, for the three specimens with different particle shapes, where Gaussian fitting $f(x,\ \mu,\ \sigma) = 1/[(2\pi)^{0{\cdot}5}\sigma]\ \exp[-(x-\mu)^2/(2\sigma^2)]$ and Weibull fitting $f(x, \lambda, k) = k/\lambda(x/\lambda)^{(k-1)}\ \exp[-(x/\lambda)^k]$ are performed. It can be seen that K_n shares a probability distribution similar to k_s, whereas the distribution of k_s is wider and shorter (i.e. with larger μ and σ). It is worth noting that the distribution of contact stiffness within specimen G3-HM can be better fitted by a Weibull distribution, which is slightly different from the other two specimens. The authors note here that such a difference is associated with complexity of particle shape. Quantitatively, the mean of k_s is slightly larger than the mean of K_n with a ratio of approximate 1·2, where both means approximately lie between $3{\sim}4 \times 10^5$ N/m ($\sim r_0 \times 1$ GPa) regardless of particle shape effect. Yimsiri & Soga (2000) pointed out that a small discrepancy between K_n and k_s in the LS model would not significantly affect the mechanical behaviours of a granular material. Therefore, that tangential contact stiffness is set equal to normal contact stiffness in the LS model is reasonable to some degree. Moreover, given that the contact stiffness in the HM model is penetration-dependent, it is not surprising to see that the probability distribution of contact stiffness moves right and becomes wider after shearing. The corresponding mean does not exceed 6×10^5 N/m for all specimens. Also, the shifted distributions have similar characteristics for all specimens. That is to say, the probability distribution of contact stiffness is strongly sensitive to the stress state, but not to particle shape.

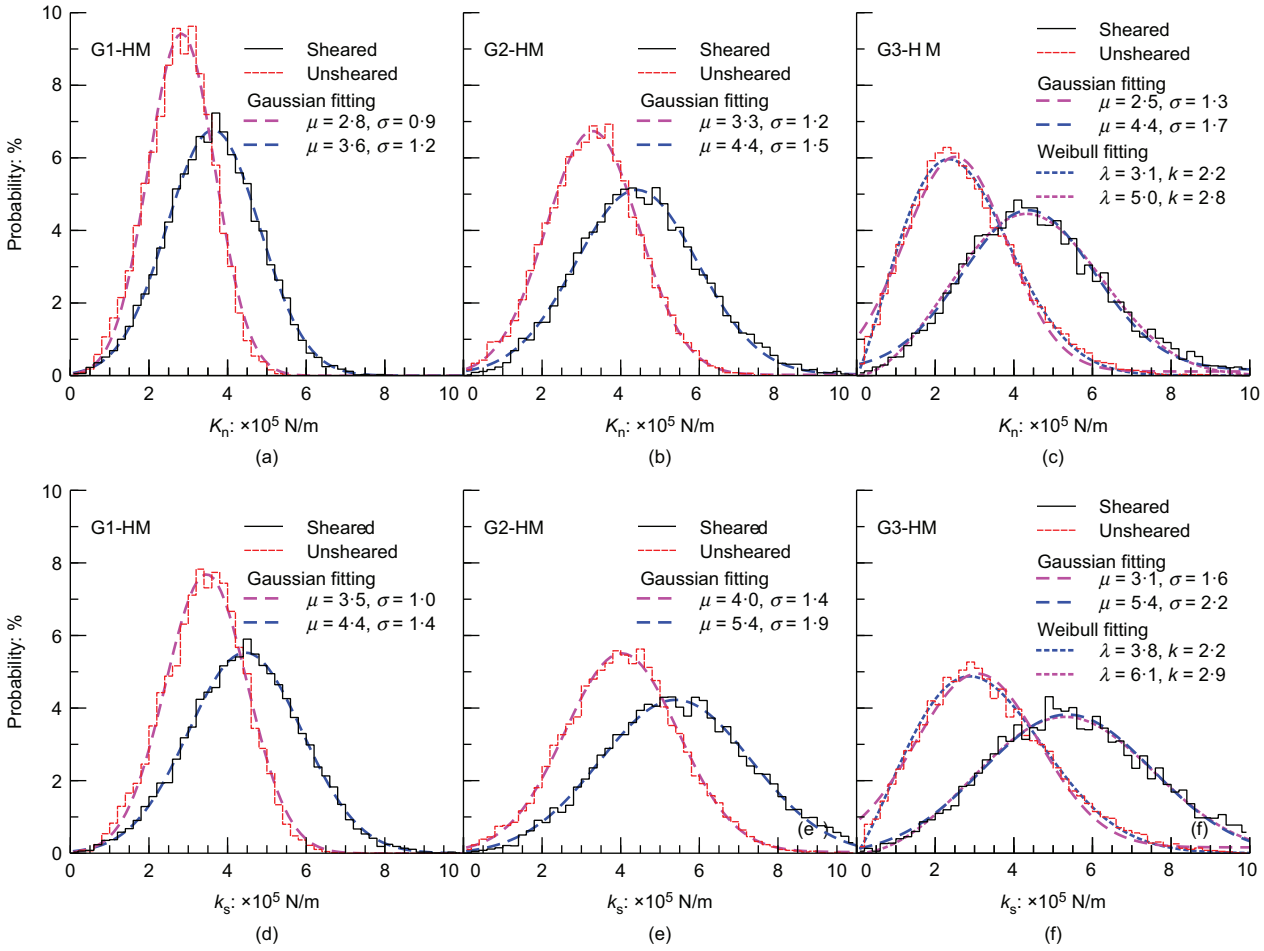

Fig. 6. Histograms of (a), (b), (c) normal-secant and (d), (e), (f) shear-tangential stiffnesses for specimens G*i*-HM before and after shearing

Local void ratio distributions. The void space distribution is related to deformation behaviour, stress state and conduction phenomena within granular media (Jowitt & Munro, 1975; Kang *et al.*, 2014). To date, several schemes have been employed to quantify void space within a granular material – for example, Oda (1977) and Kang *et al.* (2014). Herein, a typical approach is adopted – namely, the Voronoi tessellation – to weigh local voids to each individual particle, where an individual particle is enclosed by a Voronoi cell. This method has been widely applied to sphere packings – for example, Evans & Brown (2014), Yi *et al.* (2015) and Zhao *et al.* (2017a) – but to just a few non-spherical particles (Luchnikov *et al.*, 1999; Baule *et al.*, 2013; Schaller *et al.*, 2015) owing to the complication of construction of Voronoi cells. A recently developed technique, set Voronoi tessellation (Schaller *et al.*, 2013), is used for Voronoi cell construction for superellipsoidal particles in this work.

For each Voronoi cell and/or each particle i, local void ratio e_i is defined as the ratio of the void volume V_{v_i} to the particle volume V_{s_i}. Following the literature (Kuo & Frost, 1996; Evans & Frost, 2010), by weighting the local void ratios by their respective solid volumes, the solid volume weighted mean of the local void ratios e_{ms} is

$$e_{ms} = \frac{\sum_{i=1}^{N_p} V_{s_i} e_i}{\sum_{i=1}^{N_p} V_{s_i}} = \frac{V_v}{V_s} \tag{9}$$

where N_p is the total number of Voronoi cells. The mean of the solid volume weighted local void ratios is equal to the global void ratio by the given definition.

Figures 7(a)–7(c) and 7(d)–7(f) show solid volume weighted distributions for all specimens before and after shearing, respectively, where the dashed lines are best fits with a lognormal distribution $f(x, m, s) = 1/[(2\pi)^{0.5} sx] \exp\{-[\ln(x) + m]^2/(2s^2)\}$. Other forms of distribution functions have also been found to fit histograms of local void space in the literature – for example, gamma (Evans & Frost, 2010) and *K*-gamma (Guo & Zhao, 2014). It can be seen that the distribution of local void ratios becomes wider with an increasing mean after shearing, consistent with the corresponding dilatation. It is evident that specimens G*i*-LS1 have about the same local void distributions as specimens G*i*-HM before shearing, indicating that the initial fabric of specimens G*i*-LS1 and G*i*-HM is almost the same. However, a small discrepancy of local void distributions between specimens G*i*-LS2 and the others is observed, which is attributed to their lower contact stiffness. With respect to the sheared states, all distributions in each group are different, but not significant, indicating that while various contact models predict similar initial fabric, shearing elucidates the difference in microstructure for different contact models.

Probability distribution functions of contact forces. The probability distribution function (PDF) of contact forces is an important and common quantity to investigate the contact force network (Majmudar & Behringer, 2005). The PDFs of normal contact forces f_n normalised by the mean normal contact force $\langle f_n \rangle$ at the initial and final states are shown in Figs 8(a)–8(c) and 8(d)–8(f), respectively. It can be seen that there is a significant shear-induced variation in the PDF (Majmudar & Behringer, 2005), indicating that the

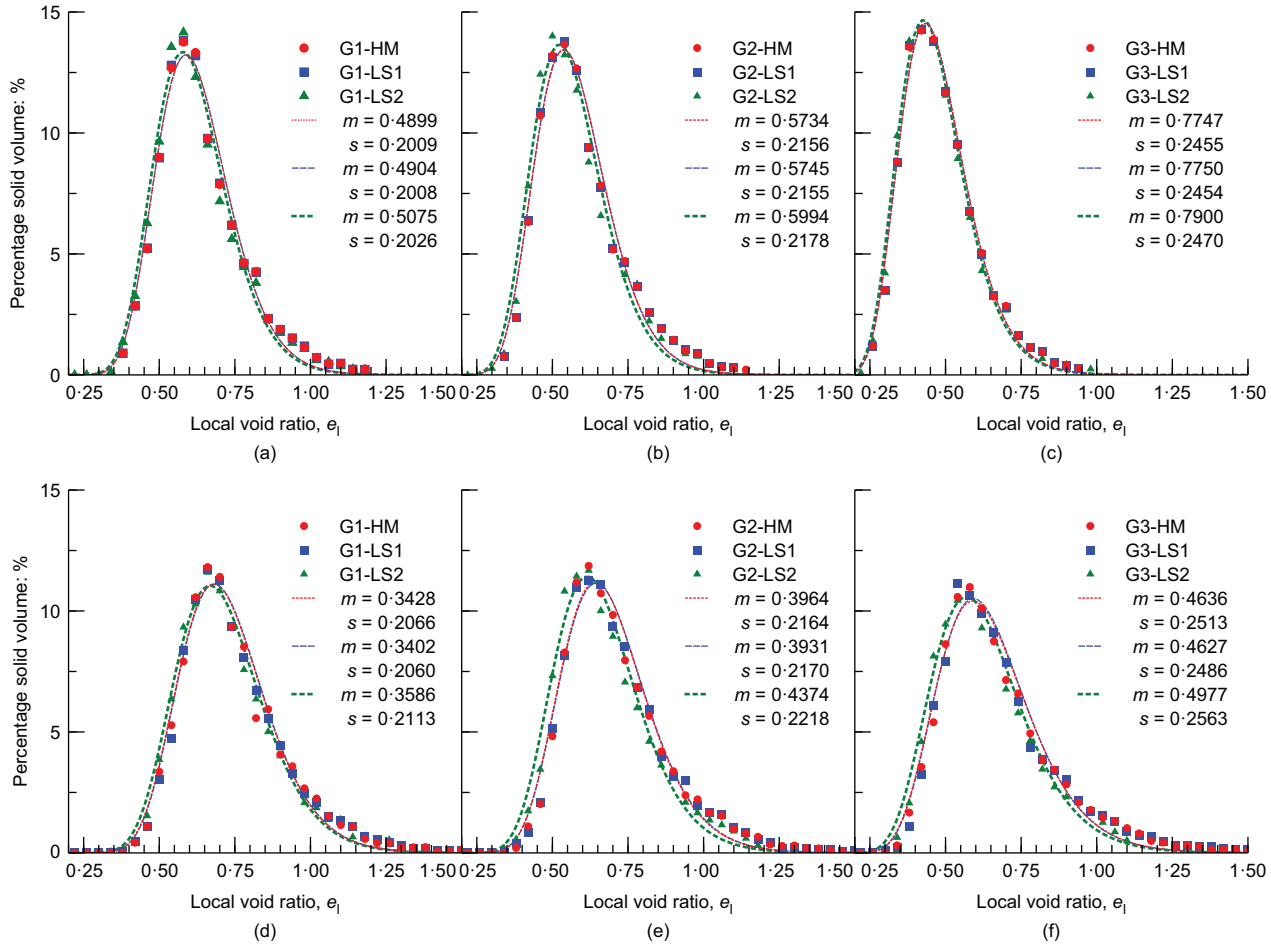

Fig. 7. Solid volume weighted distributions for (a), (b), (c) unsheared and (d), (e), (f) sheared specimens

PDF is history dependent, as reported in other literature – for example, Zhao & Zhou (2017). Furthermore, as generally observed in granular packings (Zhao *et al.*, 2017a, 2017b), the proportion of contacts with forces above the mean $\langle f_n \rangle$ decreases exponentially, whereas the proportion of contacts with forces below the mean follows a power law

$$\mathrm{PDF}(f_n) \propto \begin{cases} e^{\alpha_1 (f_n/\langle f_n \rangle)} & f_n > \langle f_n \rangle \\ \left(\dfrac{f_n}{\langle f_n \rangle} \right)^{\beta_1} & f_n < \langle f_n \rangle \end{cases} \tag{10}$$

where α_1 and β_1 are fitting parameters. It is worth pointing out that the mean normal contact force $\langle f_n \rangle$ might not be the watershed for the best fitting.

For specimens in each group, it can be seen that the contact model has a significant effect on the PDF $(f_n/\langle f_n \rangle)$ at the initial state, but not at the final state. This feature is independent of particle shape. Particularly at the initial state, the PDF $(f_n/\langle f_n \rangle)$ for specimens G*i*-LS1 is consistent with that for specimens G*i*-HM at the greatest range of f_n, indicating that the LS model is able to yield similar mechanical behaviours as the HM model at the contact scale. However, an obvious discrepancy is observed at the left tail – that is, $f_n < 0{\cdot}1 \langle f_n \rangle$. This is because the LS model with a constant stiffness overestimates the contact stiffness when using the HM model for small normal contact forces (or small penetrations). That is also why a lower probability is seen for small normal contact forces. With respect to specimens G*i*-LS2, most of the normal contact forces stay within a small range between $0{\cdot}5 \langle f_n \rangle$ and $2{\cdot}0 \langle f_n \rangle$.

Evolution of microscopic parameters

Mean normal contact force and mean coordination number. Previous studies have shown that normal contact forces within granular materials have a major contribution to undertaking the external loading (Radjaï *et al.*, 1998; Zhao & Zhou, 2017). The mean normal contact force $\langle f_n \rangle$ is defined as the average of normal contact force magnitudes over all contacts. Evolution of $\langle f_n \rangle$ for all three groups of specimens during shearing is plotted against axial strain in Figs 9(a)–(9(c)). It is not surprising that $\langle f_n \rangle$ behaves similarly to the deviatoric stress ratio, owing to its major contribution to the shear strength. Moreover, $\langle f_n \rangle$ is around 0·05 N at the initial states for all specimens, regardless of particle shape. During shearing, the mean normal contact forces in specimens G1-LS1 and G2-LS1 are well in line with that in specimen G1-HM and specimen G2-HM, repectively. However, $\langle f_n \rangle$ in specimen G3-LS1 is considerably smaller than that in specimen G3-HM, implying a non-negligible effect of particle shape on $\langle f_n \rangle$ to some extent.

The mean coordination number, Z, defined as the mean number of neighbours touching each individual particle, is an important parameter for quantifying the internal fabric of a granular assembly. As shown in Figs 9(a)–9(c), the mean coordination number shows a quick drop with axial strain before approaching a steady value, which can be regarded as a critical value. A similar trend was described by a theoretical relationship associated with granular plastic deformation in two-dimensional discrete-element simulations (Rothenburg & Kruyt, 2004). Moreover, it can be seen that specimens G*i*-LS1 and G*i*-HM share about the same evolution of Z, even though some fluctuation is observed in specimens

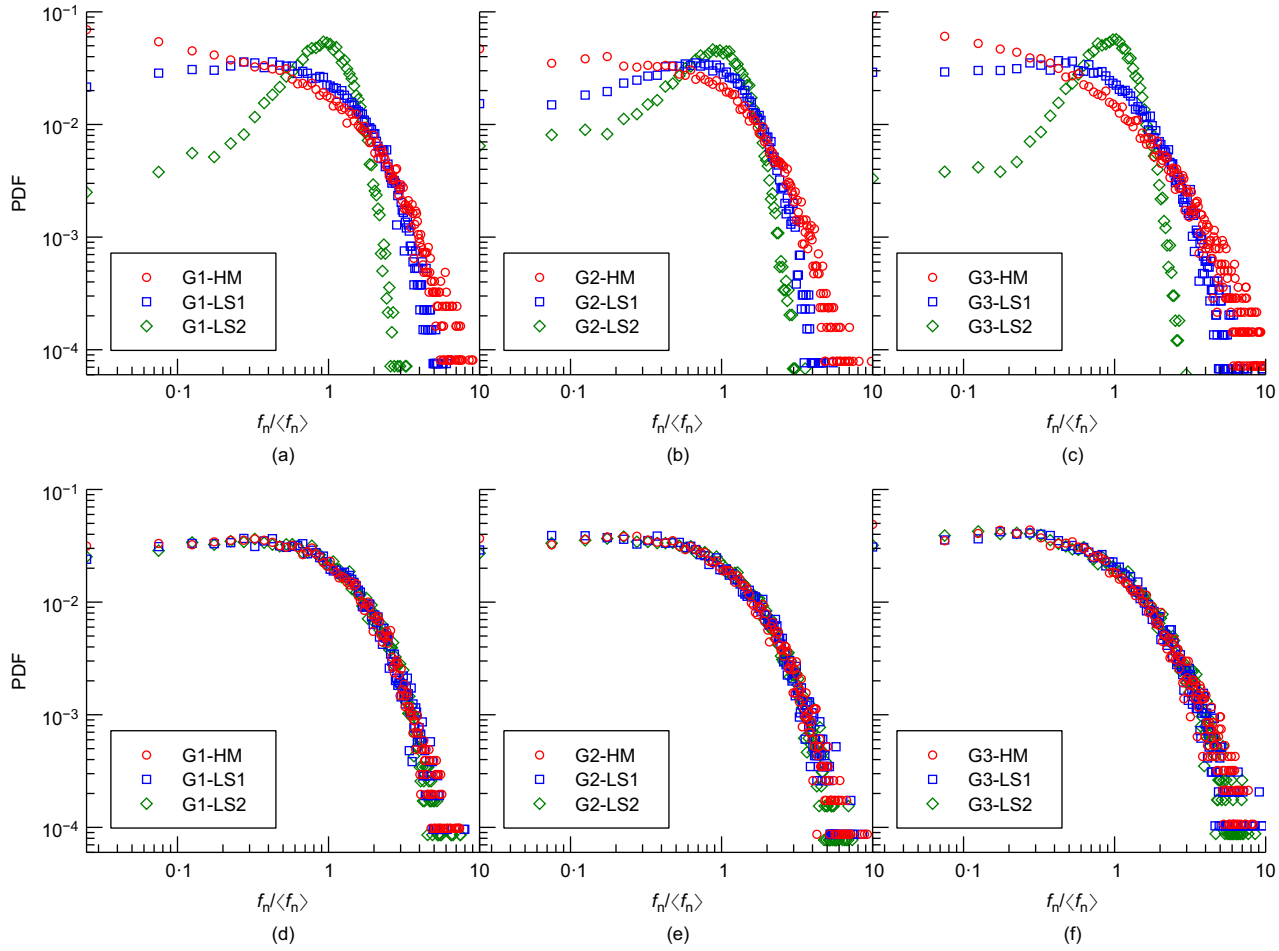

Fig. 8. Probability distribution functions of normalised normal contact forces $f_n/\langle f_n \rangle$ for (a), (b), (c) unsheared and (d), (e), (f) sheared specimens

G*i*-HM, especially in specimen G3-HM, where the fluctuation might be attributed to instability caused by diverse particle shapes. Furthermore, specimens G*i*-LS2 have much larger mean coordination numbers due to their low contact stiffness, which corresponds to smaller mean normal contact forces.

Proportions of sliding and weak contacts. It is well known that force transmission within granular materials is by way of inter-particle contacts. On one hand, contacts are mobilised to different degrees under loading, where a contact is completely mobilised when the tangential contact force reaches the maximum frictional force – that is, sliding contact. On the other hand, contacts carry large or small forces – that is, strong or weak contacts – connecting as strong or weak contact force networks to equilibrate the external loading. Strong contacts carry the whole deviatoric load while almost the whole friction dissipation occurs at weak contacts (Radjaï *et al.*, 1998; Estrada *et al.*, 2008). For simplicity, contacts carrying normal contact forces less than the mean $\langle f_n \rangle$ are denoted as weak contacts, while the others are denoted as strong contacts. It is worth pointing out that such a classification using $\langle f_n \rangle$ is rough and arbitrary because $\langle f_n \rangle$ does not correspond to a transition in the partial network (i.e. 'ξ-network' (Radjaï *et al.*, 1998)) owing to the effect of particle shape (Zhao & Zhou, 2017). However, it is fine to use $\langle f_n \rangle$ to roughly separate the strong and weak contacts for the comparison presented in the following.

Sliding contact proportion ζ_s and weak contact proportion ζ_w for all three groups of specimens were monitored during shearing as shown in Figs 10(a)–10(c). It can be seen that both ζ_s and ζ_w have a quick initial increase, then slightly decrease to a relatively steady value. Similar evolution of ζ_s and ζ_w has been reported previously (Guo & Zhao, 2013; Zhao & Zhou, 2017). Moreover, ζ_s in specimens G*i*-LS1 quantitatively agrees with that in specimens G*i*-HM, whereas ζ_s in specimens G*i*-LS2 is lower than that in specimens G*i*-LS1 and G*i*-HM. In particular, it appears that the discrepancy between specimens G*i*-LS2 and the others is related to particle shape to some degree. With respect to ζ_w, specimens G*i*-LS1 and G*i*-HM share about the same evolution of ζ_w as expected. Moreover, it is evident that contact stiffness has only a small effect on the critical value of ζ_w, which is around 60∼65% regardless of particle shape.

Anisotropy. Anisotropy is a well-known characteristic of granular materials, which attracts growing attention in the field of geomechanics. Here the focus is placed on three typical vectorial measures, namely, contact normal (orientation), branch vector and contact force, to quantify granular fabric. A contact normal is defined as the unit normal vector of the particle surface at contact, and a branch vector is defined as the vector connecting the centroids of two adjacent particles. Following the literature (Satake, 1982; Zhao *et al.*, 2017b), a rank-2 fabric tensor $\boldsymbol{\Phi}_{ij}$ of each vectorial measure $\boldsymbol{n}$ is introduced by equation (11) with the corresponding quantification of anisotropy given in equation (12).

$$\boldsymbol{\Phi}_{ij}(\boldsymbol{n}) = \frac{1}{N_c}\sum_{k=1}^{N_c} n_i^{(k)} n_j^{(k)} \tag{11}$$

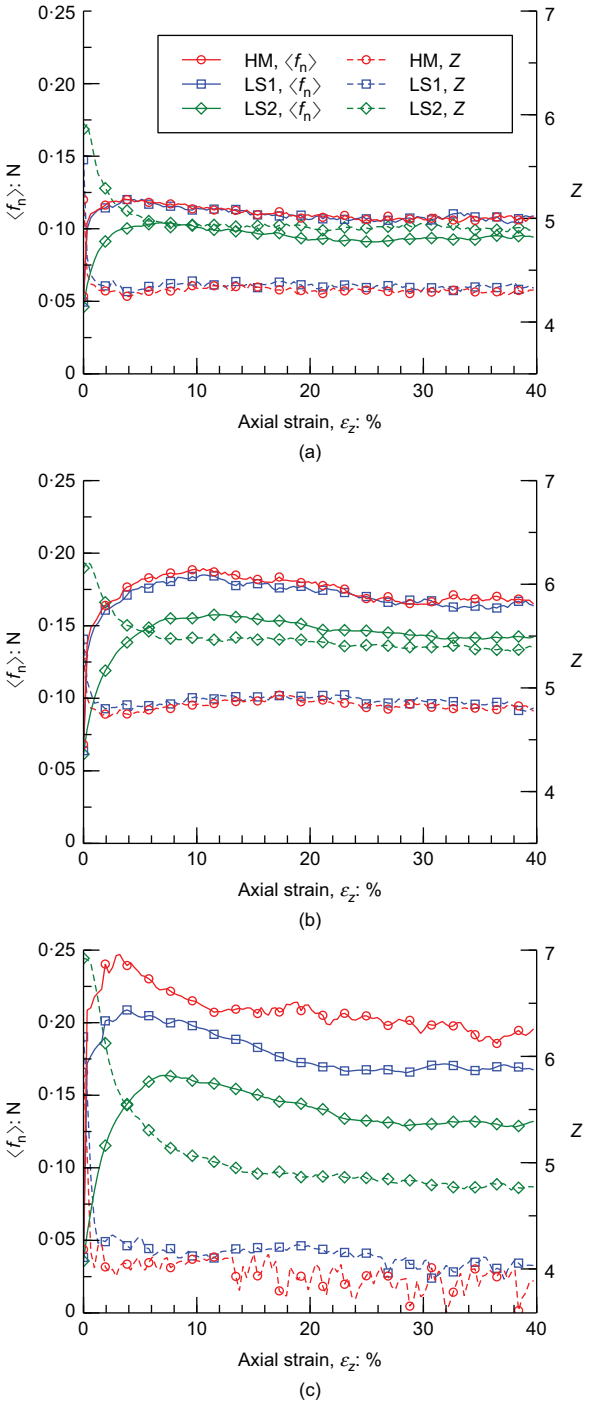

Fig. 9. Evolution of mean normal contact forces $\langle f_n \rangle$ and mean coordination numbers Z for all specimens during shearing: (a) G1; (b) G2; (c) G3

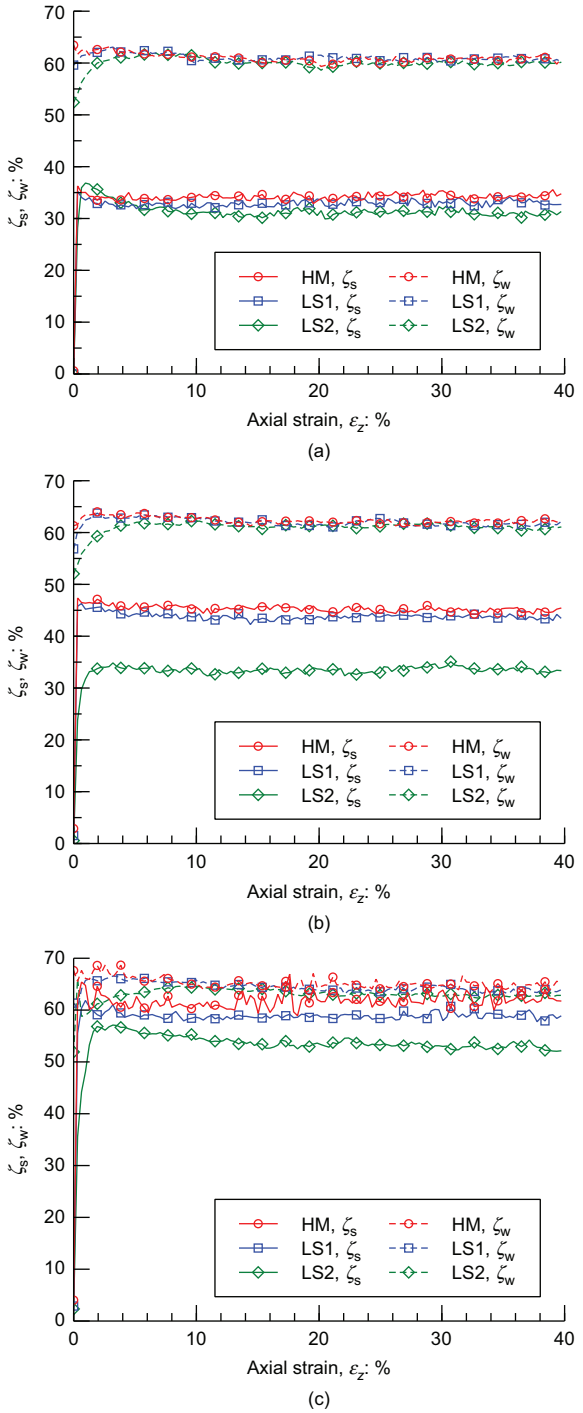

Fig. 10. Evolution of sliding contact proportion ζ_s and weak contact proportion ζ_w for all specimens during shearing: (a) G1; (b) G2; (c) G3

$$A(\boldsymbol{n}) = \sqrt{\frac{3}{2}\Phi'_{ij}\Phi'_{ij}}/\Phi_{kk} \tag{12}$$

where N_c is the total number of particle–particle contacts; Φ'_{ij} is the deviatoric part of $\boldsymbol{\Phi}_{ij}$.

Evolution of contact orientation anisotropy A_c for all three groups of specimens during shearing are shown in Figs 11(a)–11(c), where A_c exhibits a softening type similar to the evolution of deviatoric stress ratio in Fig. 4. A_c in specimens G*i*-LS1 is well in line with that in specimens G*i*-HM, and considerably greater than that in specimens G*i*-LS2. Moreover, evolution of branch vector anisotropy A_{bv} is plotted together with A_c, as shown in Figs 11(a)–11(c). Not surprisingly, A_{bv} significantly coincides with A_c for specimens with spherical particles, referring to Fig. 11(a), which is attributed to the fact that the branch vector lies along the contact normal at a sphere–sphere contact. However, for the other two groups of specimens, the difference in A_{bv} and A_c is dramatic owing to the complex particle shapes. Furthermore, with respect to contact force anisotropy A_f as shown in Fig. 12, it appears that the contact model does not have a significant effect on the respective evolution for all groups of specimens.

Other general loading conditions

The above analysis is based on axisymmetric compression – that is, $\sigma_2 = \sigma_3$ during compression. For a more

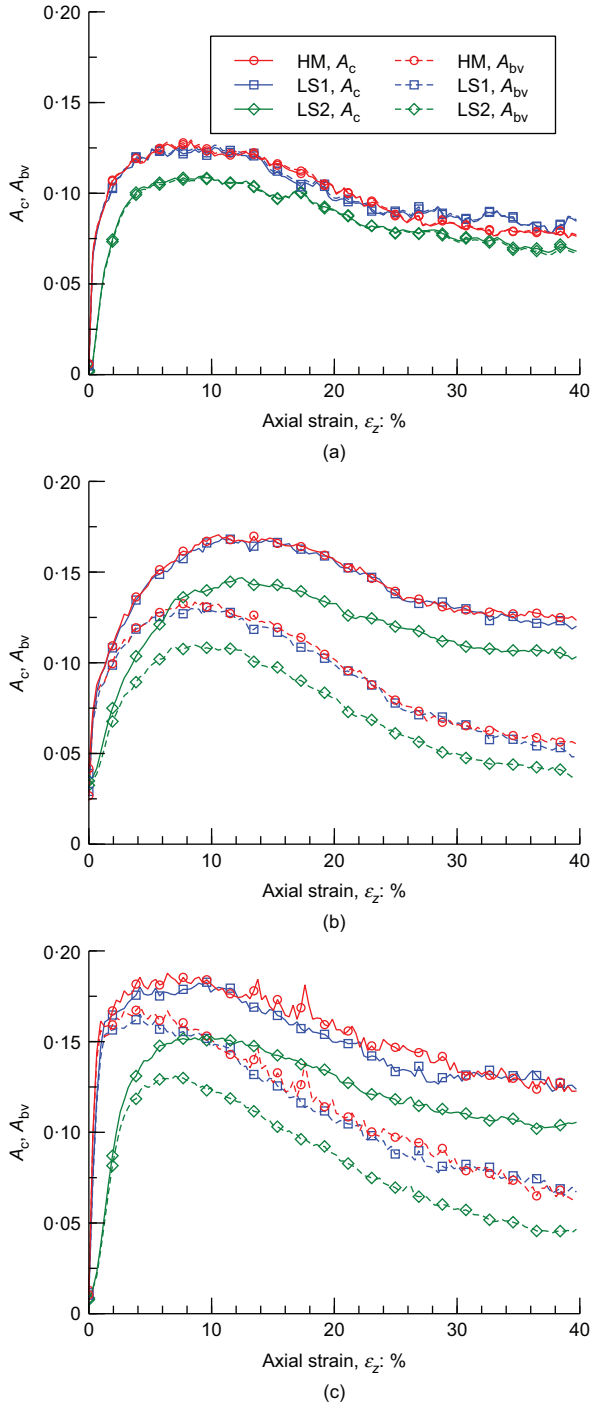

Fig. 11. Evolution of contact orientation anisotropy A_c and branch vector anisotropy A_{bv} for all specimens during shearing: (a) G1; (b) G2; (c) G3

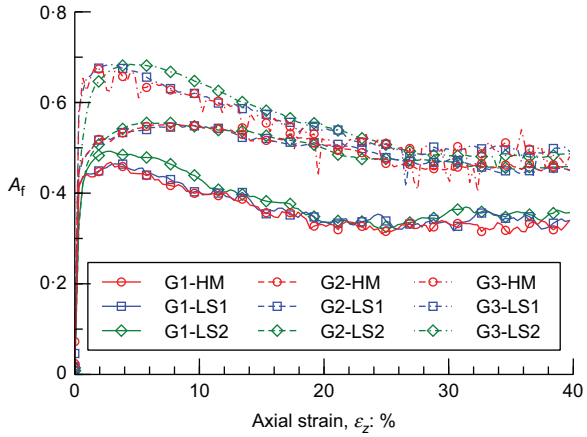

Fig. 12. Evolution of anisotropy of contact forces A_f for all specimens during shearing

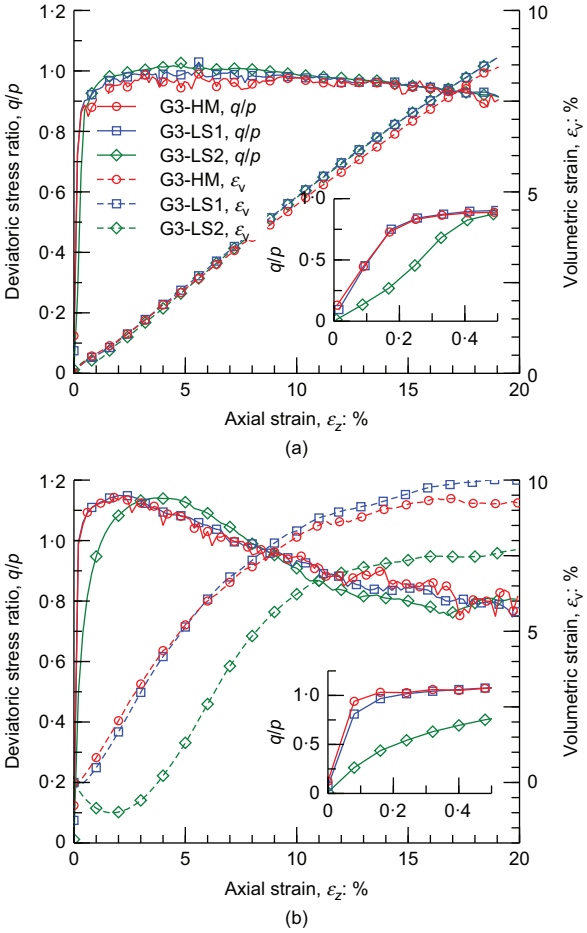

Fig. 13. Variation of deviatoric stress ratio q/p and volumetric strain ε_v during (a) triaxial extension and (b) constant-b_0 triaxial compression tests

comprehensive comparison between the HM and LS models, two additional loading conditions, namely, axisymmetric extension with $\sigma_2 = \sigma_3$ and true triaxial compression with a constant intermediate principal stress ratio $b_0 = (\sigma_2 - \sigma_3)/(\sigma_1 - \sigma_3) = 0{\cdot}5$, are performed on specimen group G3. As shown in Fig. 13(a), during the extension test, contact stiffness does not have a significant effect on q/p and ε_v except at small strains. However, for the constant-b_0 compression test, referring to Fig. 13(b), the effect of contact stiffness on q/p and ε_v is similar to that observed in the conventional compression tests. Overall, using the LS model can yield similar results to the HM model for these general loading conditions.

CONCLUSIONS

Contact stiffness has a significant effect on deformation but not on shear strength of granular assemblies, which is associated with the corresponding microscopic responses. However, the small-strain behaviours are significantly affected by contact stiffness, as discussed by Yimsiri & Soga (2000). Specimens with softer contacts show larger mean coordination numbers but smaller mean normal contact forces, regardless of particle shape, and thereby

lower proportions of sliding contacts during shearing. Moreover, the contact model does not have any considerable effect on distributions of contact forces regardless of particle shape. However, specimens with softer contacts show much more uniform distributions of contact orientations and branch vectors. Furthermore, contact stiffness distributions within specimens using the HM model are strongly sensitive to the stress state but not to particle shape.

A key finding is that the LS model is able to resemble the HM model on aspects of both microscopic and macroscopic mechanical behaviours of granular materials with spherical and/or non-spherical particles. This finding suggests that the LS model can be used to investigate micro-mechanical behaviours of granular soils with complex particle shapes. The authors note here that the computational cost can be reduced significantly for non-spherical particles by using the LS model, but not for spherical particles. Moreover, a relationship between the normal and tangential contact stiffnesses $k_n/r_0 = k_s/r_0 = 1$ GPa (r_0 is the average radius of particles) in the LS model is recommended to yield similar results as using the HM model for narrowly graded quartz sands – for example, Ottawa 20–30. Moreover, given that dynamic interactions are based on the non-linearity of contact stiffness (Mouraille & Luding, 2008), further discrepancies between the HM and LS models may arise for dynamic problems. Thus, the present results are restricted to quasistatic situations, including general loading conditions. A more comprehensive study on the criterion of normal and tangential stiffness in the LS model is worth conducting in further work, which would shed light on effects of material properties, GSDs and so forth.

ACKNOWLEDGEMENTS

This work is supported by the State Key Laboratory of Subtropical Building Science, South China University of Technology (2017KA04), and partially supported by the Water Conservancy Science and Technology Innovation Project of Guangdong Province (2015-17), Science and Technology Program of Guangzhou (201707020047) and the Science and Technology Project of Powerchina Huadong Engineering Corporation Limited (SD2013-10). The China Scholarship Council is greatly appreciated for financially supporting S. Zhao to study at Oregon State University, USA. T. M. Evans received support from the US National Science Foundation (CMMI-1538460) and the US Department of Energy (DE-FG36-08GO18179) during the course of this work. This support is gratefully acknowledged.

APPENDIX 1. HM CONTACT STIFFNESS FOR GENERAL ELASTIC PARTICLES

The contact profile of two contacting elastic bodies can be approximately regarded as an ellipse with semi-axes denoted as a and b. Contact geometry can be defined in terms of the curvature sum ρ_s and curvature difference F_ρ

$$\rho_s = \rho_I^i + \rho_{II}^i + \rho_I^j + \rho_{II}^j \tag{13}$$

$$F_\rho = \frac{1}{\rho_s}[(\rho_I^i - \rho_{II}^i)^2 + (\rho_I^j - \rho_{II}^j)^2 + 2(\rho_I^i - \rho_{II}^i)(\rho_I^j - \rho_{II}^j) \times \cos 2\omega]^{1/2} \tag{14}$$

where ρ_I and ρ_{II} are the principal curvatures at contact; the superscripts i and j denote the two contacting particles hereafter; and ω is the angle between the directions of the maximum or minimum principal curvatures of the two particles.

The relative curvatures A and B (with $B \leq A$) are obtained from

$$A = \frac{\rho_s}{4}(1 + F_\rho), \quad B = \frac{\rho_s}{4}(1 - F_\rho) \tag{15}$$

Assuming $a < b$ for convenience, two geometric parameters are introduced

$$\alpha = \frac{a}{b}, \quad e = \sqrt{1 - \alpha^2} \tag{16}$$

Therefore, the following is obtained

$$A + B = \frac{\delta E'}{a^2 K'} \tag{17}$$

$$\frac{A}{B} = \frac{(1/\alpha)^2 E' - K'}{K' - E'} \tag{18}$$

where K' and E' are the complete elliptic integrals of the first kind and the second kind of argument e, respectively, and their approximate numerical solutions are given in Appendix 2.

The normal contact force F_n at a Hertz contact is given as

$$F_n = \frac{4\pi}{3\alpha}\sqrt{\frac{E'}{(A+B)K'^3}}G^*\delta^{3/2} \tag{19}$$

where G^* is the equivalent contact shear modulus in terms of the particle shear modulus G and Poisson ratio ν, given by

$$\frac{1}{G^*} = \frac{1-\nu^i}{G^i} + \frac{1-\nu^j}{G^j} \tag{20}$$

Therefore, the corresponding contact normal-secant stiffness K_n and contact normal-tangent stiffness k_n are given as

$$K_n = \frac{F_n}{\delta} = \frac{4\pi}{3\alpha}\sqrt{\frac{E'}{K'^3(A+B)}}G^*\delta^{1/2} \tag{21}$$

$$k_n = \frac{dF_n}{d\delta} = \frac{2\pi}{\alpha}\sqrt{\frac{E'}{K'^3(A+B)}}G^*\delta^{1/2} \tag{22}$$

With Mindlin's theory (Mindlin, 1949), the no-slip solutions of contact shear tangent stiffness in the principal direction of the contact ellipse can be formularised as

$$k_x = 2\pi b\left(\mu_1 K' - \mu_2\frac{K' - E'}{e^2}\right)^{-1} \tag{23}$$

$$k_y = 2\pi b\left(\mu_1 K' + \mu_2\frac{(1-e^2)K' - E'}{e^2}\right)^{-1} \tag{24}$$

with

$$\mu_1 = \frac{1}{G^i} + \frac{1}{G^j} \quad \mu_2 = \frac{\nu^i}{G^i} + \frac{\nu^j}{G^j} \tag{25}$$

The key to solve equations (21)–(24) is to compute the semi-axis ratio α, which can be numerically solved as shown in Appendix 3.

APPENDIX 2. NUMERICAL APPROXIMATE SOLUTIONS OF THE COMPLETE ELLIPTIC INTEGRALS

The complete elliptic integrals of the first kind K' and the second kind E' are defined as

$$K'(e) = \int_0^{\pi/2}\frac{d\theta}{\sqrt{1 - e^2\sin^2(\theta)}} \tag{26a}$$

$$E'(e) = \int_0^{\pi/2}\sqrt{1 - e^2\sin^2(\theta)}d\theta \tag{26b}$$

Table 4. Fitting parameters for equations (27) and (29)

α_1	1·3862944	β_1	1·0	γ_1	0·40227436
α_2	0·1119723	β_2	0·4630151	γ_2	$3{\cdot}7491752 \times 10^{-2}$
α_3	0·0725296	β_3	0·1077812	γ_3	$7{\cdot}4855761 \times 10^{-4}$
α_4	0·5	β_4	0·2452727	γ_4	$2{\cdot}1667028 \times 10^{-6}$
α_5	0·1213478	β_5	0·0412496	γ_5	0·42678878
α_6	0·0288729			γ_6	$4{\cdot}2605401 \times 10^{-2}$
				γ_7	$9{\cdot}0786922 \times 10^{-4}$
				γ_8	$2{\cdot}7868927 \times 10^{-6}$

which can be approximately expressed as follows (Abramowitz & Stegun, 1972)

$$K'(e) = \alpha_1 + \alpha_2 e_1 + \alpha_3 e_1^2 - (\alpha_4 + \alpha_5 e_1 + \alpha_6 e_1^2)\ln(e_1) \tag{27a}$$

$$E'(e) = \beta_1 + \beta_2 e_1 + \beta_3 e_1^2 - (\beta_4 e_1 + \beta_5 e_1^2)\ln(e_1) \tag{27b}$$

where $e_1 = 1 - e_2$, and $\alpha_1 \ldots \alpha_6$ and $\beta_1 \ldots \beta_5$ are fitting parameters listed in Table 4. According to (Abramowitz & Stegun, 1972), the absolute errors of K' and E' do not exceed 3×10^{-5} and 4×10^{-5}, respectively.

APPENDIX 3. NUMERICAL APPROXIMATE SOLUTIONS OF THE SEMI-AXIS RATIO

The semi-axis ratio α is an implicit function of the mean curvatures of the two touching particles in equation (18), which can be approximately represented as a function of the ratio of the two relative curvatures $\beta = A/B$, that is

$$\alpha = \beta^{\gamma} \tag{28}$$

where γ is a function of β (Antoine *et al.*, 2006) defined as

$$\gamma = \frac{-2(1 + \gamma_1 x + \gamma_2 x^2 + \gamma_3 x^3 + \gamma_4 x^4)}{3(1 + \gamma_5 x + \gamma_6 x^2 + \gamma_7 x^3 + \gamma_8 x^4)} \tag{29}$$

in which $x = \log_{10}^{2}(\beta)$ and $\gamma_1 \ldots \gamma_8$ are fitting parameters listed in Table 4. According to Antoine *et al.* (2006), the absolute error of α does not exceed $5{\cdot}86 \times 10^{-6}$ for $10^{-8} \leq \alpha \leq 10^{8}$.

APPENDIX 4. PRINCIPAL CURVATURES OF A SUPERELLIPSOID

The parametric function of a superellipsoid

$$R(\theta,\phi) = \begin{bmatrix} \mathrm{Sign}(\cos\theta) r_x |\cos\theta|^{\epsilon_1} |\cos\phi|^{\epsilon_2} \\ \mathrm{Sign}(\sin\theta) r_y |\sin\theta|^{\epsilon_1} |\cos\phi|^{\epsilon_2} \\ \mathrm{Sign}(\sin\phi) r_z |\sin\phi|^{\epsilon_2} \end{bmatrix} \tag{30}$$

with $\theta \in [0, 2\pi)$, $\phi \in [-\pi/2, \pi/2]$ where r_x, r_y and r_z are semi-lengths along the principal directions at the body-fixed coordinate system. The term $\mathrm{Sign}(x)$ is the signum function.

Therefore, the first and second derivatives are derived as the following

$$R_\theta = \begin{bmatrix} -\mathrm{Sign}(\cos\theta) r_x \epsilon_1 |\cos\theta|^{\epsilon_1 - 2} |\cos\phi|^{\epsilon_2} \cos\theta \sin\theta \\ \mathrm{Sign}(\sin\theta) r_y \epsilon_1 |\sin\theta|^{\epsilon_1 - 2} |\cos\phi|^{\epsilon_2} \cos\theta \sin\theta \\ 0 \end{bmatrix} \tag{31}$$

$$R_\phi = \begin{bmatrix} -\mathrm{Sign}(\cos\theta) r_x \epsilon_2 |\cos\theta|^{\epsilon_1} |\cos\phi|^{\epsilon_2 - 2} \cos\phi \sin\phi \\ -\mathrm{Sign}(\sin\theta) r_y \epsilon_2 |\sin\theta|^{\epsilon_1} |\cos\phi|^{\epsilon_2 - 2} \cos\phi \sin\phi \\ \mathrm{Sign}(\sin\phi) r_z \epsilon_2 |\sin\phi|^{\epsilon_2 - 2} \cos\phi \sin\phi \end{bmatrix} \tag{32}$$

$$R_{\theta\phi} = \cos\theta \sin\theta \cos\phi \sin\phi \times \begin{bmatrix} \mathrm{Sign}(\cos\theta) r_x \epsilon_1 \epsilon_2 |\cos\theta|^{\epsilon_1 - 2} |\cos\phi|^{\epsilon_2 - 2} \\ -\mathrm{Sign}(\sin\theta) r_y \epsilon_1 \epsilon_2 |\sin\theta|^{\epsilon_1 - 2} |\cos\phi|^{\epsilon_2 - 2} \\ 0 \end{bmatrix} \tag{33}$$

$$R_{\theta\theta} = \begin{bmatrix} \mathrm{Sign}(\cos\theta) r_x \epsilon_1 |\cos\theta|^{\epsilon_1 - 2} |\cos\phi|^{\epsilon_2} (\epsilon_1 \sin^2\theta - 1) \\ \mathrm{Sign}(\sin\theta) r_y \epsilon_1 |\sin\theta|^{\epsilon_1 - 2} |\cos\phi|^{\epsilon_2} (\epsilon_1 \cos^2\theta - 1) \\ 0 \end{bmatrix} \tag{34}$$

$$R_{\phi\phi} = \begin{bmatrix} \mathrm{Sign}(\cos\theta) r_x \epsilon_2 |\cos\theta|^{\epsilon_1} |\cos\phi|^{\epsilon_2 - 2} (\epsilon_2 \sin^2\phi - 1) \\ \mathrm{Sign}(\sin\theta) r_y \epsilon_2 |\sin\theta|^{\epsilon_1} |\cos\phi|^{\epsilon_2 - 2} (\epsilon_2 \sin^2\phi - 1) \\ \mathrm{Sign}(\sin\phi) r_z \epsilon_2 |\sin\phi|^{\epsilon_2 - 2} (\epsilon_2 \cos^2\phi - 1) \end{bmatrix} \tag{35}$$

The unit normal vector of the surface is

$$\boldsymbol{n} = \frac{R_\theta \times R_\phi}{|R_\theta \times R_\phi|} \tag{36}$$

where '$\times$' denotes a vector cross product, and '$|\,|$' is for a vector norm.

The first fundamental form coefficients

$$E_1 = R_\theta \cdot R_\theta \quad F_1 = R_\theta \cdot R_\phi \quad G_1 = R_\phi \cdot R_\phi \tag{37}$$

where '$\cdot$' is for a vector dot product.

The second fundamental form coefficients

$$L_1 = R_{\theta\theta} \cdot \boldsymbol{n} \quad M_1 = R_{\theta\phi} \cdot \boldsymbol{n} = 0 \quad N_1 = R_{\phi\phi} \cdot \boldsymbol{n} \tag{38}$$

Gaussian curvature

$$P = \frac{L_1 N_1}{E_1 G_1 - F_1^2} \tag{39}$$

Mean curvature

$$Q = \frac{E_1 N_1 + G_1 L_1}{2(E_1 G_1 - F_1^2)} \tag{40}$$

The principal curvatures

$$\rho_{\mathrm{I}} = Q + \sqrt{Q^2 - P} \quad \rho_{\mathrm{II}} = Q - \sqrt{Q^2 - P} \tag{41}$$

NOTATION

A, B	relative curvatures
A_{bv}	anisotropy of branch vectors
A_{c}	anisotropy of contact normal (orientations)
A_{f}	anisotropy of contact forces
a, b, α, e	geometric parameters of a contact ellipse
b_0	intermediate principal stress ratio
E_1, F_1, G_1	first fundamental form coefficients
E_{c}	Young's modulus of particle
e_i	local void ratio
e_{l}, e_{ms}	local void ratio and its solid weighted mean
F_{n}	normal contact force
F_{s}	shear contact force at the current time step
F_{s}'	shear contact force at the previous time step
f^{c}	contact force at the contact c
f_{n}	normal contact force within a specimen
$\langle f_{\mathrm{n}} \rangle$	mean normal contact force
G^*	equivalent contact shear modulus
G^i	shear modulus of particle i
H	height of specimen during shearing
H_0	initial height of specimen before shearing
h	successive values of the specimen height as it changes
K', E'	complete elliptic integrals
K_{n}	normal-secant stiffness
k_{n}	normal-tangent stiffness
k_{s}	shear-tangent stiffness
k_x, k_y	principal contact shear-tangent stiffness
L_1, M_1, N_1	second fundamental form coefficients
$\boldsymbol{l}^{\mathrm{c}}$	branch vector joining the centres of the two contacting particles at contact c
m	minus mean of natural logarithm of e_{l}
N_{c}	total number of inter-particle contacts
N_{p}	total number of particles or Voronoi cells
$\boldsymbol{n}$	vectorial measure

P Gaussian curvature
p mean stress
Q mean curvature
q deviatoric stress
R radius of spherical particle
$R(\theta, \phi)$ parametric function of a superellipsoid
R_θ, R_ϕ first derivatives of $R(\theta, \phi)$
$R_{\theta\phi}$, $R_{\theta\theta}$, $R_{\phi\phi}$ second derivatives of $R(\theta, \phi)$
r, r_0 particle equivalent radius and its average
r_x, r_y, r_z semi-axis length of a superellipsoid
s standard deviation of natural logarithm of e_1
V volume of specimen during shearing
V_{s_i} particle volume within Voronoi cell i
V_{v_i} void volume within Voronoi cell i
V_0 initial volume of specimen before shearing
v successive values of the specimen volume as it changes
Z mean coordination number
α_1, β_1 fitting parameters in equation (10)
Δu incremental shear displacement
δ contact penetration depth
ε, η shape parameters of a superellipsoid
ε_v volumetric strain of a specimen
ε_x, ε_y, ε_z strains in x, y and z axes of a specimen
ε_1, ε_2 shape parameters of a superellipsoid
ζ_s proportion of sliding contacts
ζ_w proportion of weak contacts
μ_p inter-particle coefficient of friction
μ_1, μ_2 parameters in equation (25)
ν^i Poisson ratio of particle i
ρ_I, ρ_{II} principal curvatures
$\boldsymbol{\sigma}_{ij}$ stress tensor within a specimen
ρ_s, F_ρ curvature sum and curvature difference
σ'_{ij} deviatoric part of a stress tensor
$\boldsymbol{\Phi}_{ij}$ fabric tensor of a vectorial measure
Φ'_{ij} deviatoric part of a fabric tensor
ω principal curvature angle

REFERENCES

Abramowitz, M. & Stegun, I. A. (1972). *Handbook of mathematical functions with formulas, graphs and mathematical tables*, 9th edn. New York, NY, USA: Dover.

Antoine, J. F., Visa, C., Sauvey, C. & Abba, G. (2006). Approximate analytical model for Hertzian elliptical contact problems. *J. Tribol.* **128**, No. 3, 660–664.

Barr, A. H. (1981). Superquadrics and angle-preserving transformations. *IEEE Comput. Graphics Applic.* **1**, No. 1, 11–23.

Baule, A., Mari, R., Bo, L., Portal, L. & Makse, H. A. (2013). Meanfield theory of random close packings of axisymmetric particles. *Nature Communs* **4**, No. 1, 2194.

Cho, G. C., Dodds, J. & Santamarina, J. C. (2006). Particle shape effects on packing density, stiffness, and strength: natural and crushed sands. *J. Geotech. Geoenviron. Engng* **132**, No. 5, 591–602.

Christoffersen, J., Mehrabadi, M. & Nemat-Nasser, S. (1981). A micromechanical description of granular material behavior. *J. Appl. Mech.* **48**, No. 2, 339–344.

Cleary, P. W. (2008). The effect of particle shape on simple shear flows. *Powder Technol.* **179**, No. 3, 144–163.

Cui, L. & O'Sullivan, C. (2006). Exploring the macro- and microscale response of an idealised granular material in the direct shear apparatus. *Géotechnique* **56**, No. 7, 455–468, https://doi.org/10.1680/geot.2006.56.7.455.

Cui, L., O'Sullivan, C. & O'Neill, S. (2007). An analysis of the triaxial apparatus using a mixed boundary three-dimensional discrete element model. *Géotechnique* **57**, No. 10, 831–844, https://doi.org/10.1680/geot.2007.57.10.831.

Cundall, P. (1988). Computer simulations of dense sphere assemblies. In *Micromechanics of granular materials* (eds M. Satake and J. T. Jenkins), vol. 20, pp. 113–123. Amsterdam, the Netherlands: Elsevier.

Cundall, P. A. & Strack, O. D. (1979). A discrete numerical model for granular assemblies. *Géotechnique* **29**, No. 1, 47–65, https://doi.org/10.1680/geot.1979.29.1.47.

Delaney, G. W. & Cleary, P. W. (2010). The packing properties of superellipsoids. *EPL (Europhys. Lett.)* **89**, No. 3, 34002.

Di Renzo, A. & Di Maio, F. P. (2004). Comparison of contact-force models for the simulation of collisions in DEM-based granular flow codes. *Chem. Engng Sci.* **59**, No. 3, 525–541.

Eliáš, J. (2014). Simulation of railway ballast using crushable polyhedral particles. *Powder Technol.* **264**, 458–465.

Estrada, N., Taboada, A. & Radjaï, F. (2008). Shear strength and force transmission in granular media with rolling resistance. *Phys. Rev. E* **78**, No. 2, 021301.

Evans, T. M. & Brown, C. B. (2014). Microstates and macrostructures for granular assemblies. In *Geo-congress 2014 technical papers: geo-characterization and modeling for sustainability* (eds M. Abu-Farsakh, X. Yu and L. R. Hoyos), Geotechnical Special Publication 234, pp. 2858–2866. Reston, VA, USA: American Society of Civil Engineers.

Evans, T. M. & Frost, J. D. (2010). Multiscale investigation of shear bands in sand: physical and numerical experiments. *Int. J. Numer. Analyt. Methods Geomech.* **34**, No. 15, 1634–1650.

Garcia, X., Latham, J. P., Xiang, J. S. & Harrison, J. (2009). A clustered overlapping sphere algorithm to represent real particles in discrete element modelling. *Géotechnique* **59**, No. 9, 779–784, https://doi.org/10.1680/geot.8.T.037.

Goldenberg, C. & Goldhirsch, I. (2005). Friction enhances elasticity in granular solids. *Nature* **435**, No. 7039, 188–191.

Guo, N. & Zhao, J. (2013). The signature of shear-induced anisotropy in granular media. *Comput. Geotech.* **47**, 1–15.

Guo, N. & Zhao, J. (2014). Local fluctuations and spatial correlations in granular flows under constant-volume quasistatic shear. *Phys. Rev. E* **89**, No. 4, 042208.

Herrmann, H. J., Hovi, J. P. & Luding, S. (2013). *Physics of dry granular media*. Dordrecht, the Netherlands: Springer.

Höhner, D., Wirtz, S. & Scherer, V. (2012). A numerical study on the influence of particle shape on hopper discharge within the polyhedral and multi-sphere discrete element method. *Powder Technol.* **226**, 16–28.

Iwashita, K. & Oda, M. (1998). Rolling resistance at contacts in simulation of shear band development by DEM. *J. Engng Mech.* **124**, No. 3, 285–292.

Jiang, M., Shen, Z. & Wang, J. (2015). A novel three-dimensional contact model for granulates incorporating rolling and twisting resistances. *Comput. Geotech.* **65**, 147–163.

Johnson, K. (1985). *Contact mechanics*. London, UK: Cambridge University Press.

Jowitt, P. & Munro, J. (1975). The influence of void distribution and entropy on the engineering properties of granular media. In *Proceedings: applications of statistics and probability in soil and structural engineering, 2nd international conference* (ed. E. Schultze), pp. 365–385. Essen, Germany: Deutsche Gesellschaft für Erd- und Grundbau.

Kang, D. H., Yun, T. S. & Evans, T. M. (2014). Pore orientation of granular materials during biaxial compression. *Comput. Geotech.* **59**, 1–11.

Kuo, C. Y. & Frost, J. D. (1996). Uniformity evaluation of cohesionless specimens using digital image analysis. *J. Geotech. Engng* **122**, No. 5, 390–396.

Langston, P., Kennedy, A. R. & Constantin, H. (2015). Discrete element modelling of flexible fibre packing. *Comput. Mater. Sci.* **96**, 108–116.

Lin, X. & Ng, T. T. (1997). A three-dimensional discrete element model using arrays of ellipsoids. *Géotechnique* **47**, No. 2, 319–329, https://doi.org/10.1680/geot.1997.47.2.319.

Luchnikov, V., Medvedev, N., Oger, L. & Troadec, J. P. (1999). Voronoi–Delaunay analysis of voids in systems of nonspherical particles. *Phys. Rev. E* **59**, No. 6, 7205.

Majidi, B., Melo, J., Fafard, M., Ziegler, D. & Alamdari, H. (2015). Packing density of irregular shape particles: DEM simulations applied to anode-grade coke aggregates. *Advd Powder Technol.* **26**, No. 4, 1256–1262.

Majmudar, T. S. & Behringer, R. P. (2005). Contact force measurements and stress-induced anisotropy in granular materials. *Nature* **435**, No. 7045, 1079–1082.

Mindlin, R. (1949). Compliance of elastic bodies in contact. *J. Appl. Mech.* **16**, No. 3, 259–268.

Mouraille, O. & Luding, S. (2008). Sound wave propagation in weakly polydisperse granular materials. *Ultrasonics* **48**, No. 67, 498–505.

Nardelli, V., Coop, M., Andrade, J. & Paccagnella, F. (2017). An experimental investigation of the micromechanics of Eglin sand. *Powder Technol.* **312**, 166–174.

Ng, T. T. (2006). Input parameters of discrete element methods. *J. Engng Mech.* **132**, No. 7, 723–729.

Oda, M. (1977). *Fabrics and their effects on the deformation behaviors of sand*, Special Issue. Saitama, Japan: Department of Foundation Engineering, Faculty of Engineering, Saitama University.

O'Sullivan, C. (2011). Particle-based discrete element modeling: geomechanics perspective. *Int. J. Geomech.* **11**, No. 6, 449–464.

Potyondy, D. & Cundall, P. (2004). A bonded-particle model for rock. *Int. J. Rock Mech. Min. Sci.* **41**, No. 8, 1329–1364.

Radjaï, F., Wolf, D. E., Jean, M. & Moreau, J. J. (1998). Bimodal character of stress transmission in granular packings. *Phys. Rev. Lett.* **80**, No. 1, 61.

Rothenburg, L. & Kruyt, N. (2004). Critical state and evolution of coordination number in simulated granular materials. *Int. J. Solids Structs* **41**, No. 21, 5763–5774.

Santamarina, J. C., Klein, A. & Fam, M. A. (2001). *Soils and waves: particulate materials behavior, characterization and process monitoring*. Chichester, UK: Wiley.

Satake, M. (1982). Fabric tensor in granular materials. *Proceedings of the IUTAM symposium on deformation and failure of granular materials*, Delft, the Netherlands, pp. 63–68.

Schaller, F. M., Kapfer, S. C., Evans, M. E., Hoffmann, M. J., Aste, T., Saadatfar, M., Mecke, K., Delaney, G. W. & Schröder-Turk, G. E. (2013). Set Voronoi diagrams of 3D assemblies of aspherical particles. *Phil. Mag.* **93**, No. 31–33, 3993–4017.

Schaller, F. M., Neudecker, M., Saadatfar, M., Delaney, G. W., Schröder-Turk, G. E. & Schröter, M. (2015). Local origin of global contact numbers in frictional ellipsoid packings. *Phys. Rev. Lett.* **114**, No. 15, 158001.

Senetakis, K., Coop, M. R. & Todisco, M. C. (2013). The inter-particle coefficient of friction at the contacts of Leighton Buzzard sand quartz minerals. *Soils Found.* **53**, No. 5, 746–755.

Shin, H. & Santamarina, J. (2012). Role of particle angularity on the mechanical behavior of granular mixtures. *J. Geotech. Geoenviron. Engng* **139**, No. 2, 353–355.

Thornton, C. (2000). Numerical simulations of deviatoric shear deformation of granular media. *Géotechnique* **50**, No. 1, 43–53, https://doi.org/10.1680/geot.2000.50.1.43.

Thornton, C., Cummins, S. J. & Cleary, P. W. (2013). An investigation of the comparative behaviour of alternative contact force models during inelastic collisions. *Powder Technol.* **233**, 30–46.

Wellmann, C., Lillie, C. & Wriggers, P. (2008). Comparison of the macroscopic behavior of granular materials modeled by different constitutive equations on the micro scale. *Finite Elements in Analysis and Design* **44**, No. 5, 259–271.

Williams, J. R. & Pentland, A. P. (1992). Superquadrics and modal dynamics for discrete elements in interactive design. *Engng Comput.* **9**, No. 2, 115–127.

Yi, L., Dong, K., Zou, R. & Yu, A. (2015). Radical tessellation of the packing of spheres with a log-normal size distribution. *Phys. Rev. E* **92**, No. 3, 032201.

Yimsiri, S. & Soga, K. (2000). Micromechanics-based stress–strain behaviour of soils at small strains. *Géotechnique* **50**, No. 5, 559–571, https://doi.org/10.1680/geot.2000.50.5.559.

Zhao, X. & Evans, T. M. (2011). Numerical analysis of critical state behaviors of granular soils under different loading conditions. *Granular Matter* **13**, No. 6, 751–764.

Zhao, J. & Guo, N. (2013). Unique critical state characteristics in granular media considering fabric anisotropy. *Géotechnique* **63**, No. 8, 695–704, https://doi.org/10.1680/geot.12.P.040.

Zhao, S. & Zhou, X. (2017). Effects of particle asphericity on the macro-and micro-mechanical behaviors of granular assemblies. *Granular Matter* **19**, No. 2, 38.

Zhao, S., Zhou, X. & Liu, W. (2015). Discrete element simulations of direct shear tests with particle angularity effect. *Granular Matter* **17**, No. 6, 793–806.

Zhao, S., Evans, T. M., Zhou, X. & Zhou, S. (2017a). Discrete element method investigation on thermally-induced shakedown of granular materials. *Granular Matter* **19**, No. 1, 11.

Zhao, S., Zhang, N., Zhou, X. & Zhang, L. (2017b). Particle shape effects on fabric of granular random packing. *Powder Technol.* **310**, 175–186.

Zhou, B., Huang, R., Wang, H. & Wang, J. (2013). DEM investigation of particle anti-rotation effects on the micromechanical response of granular materials. *Granular Matter* **15**, No. 3, 315–326.